Recovery of light oil by medium temperature oxidation

A.A. Mailybaev[*], J. Bruining[†], D. Marchesin[‡]

Abstract

We study one aspect of combustion in porous media for the recovery of light oil. We assume that there is a temperature range above low temperature combustion where oxygen is added to the aliphatic oils to form oxygenated compounds and below the temperature where cracking and coke formation occurs. In the intermediate range oil is combusted to form small combustion products like water, CO_2, or CO. We call this medium temperature oxidation (MTO). Our simplified model considers light oil recovery when it is displaced by air at medium pressures in linear geometry, for the case when water is absent. The resulting MTO combustion displaces all the oil. There are adjacent vaporization and combustion zones, traveling with the same speed. The MTO reaction is assumed to be slow, so that vaporization is much faster. The solution of the model equations leads to a thermal wave upstream, a MTO wave in the middle and a cold isothermal Buckley-Leverett gas displacement process downstream. One of the unexpected result is that vaporization occurs upstream of the combustion zone. In the initial period the recovery curve is similar to gas displacement, but after a critical amount of air has been injected the cumulative oil recovery increases linearly until all oil has been recovered. In our model, the oil recovery is independent of reaction rate parameters, but the recovery is much faster than for gas displacement. Finally the recovery is slower for higher boiling point and higher oil viscosity, but faster at higher injection pressure. We give a simple engineering procedure to compute recovery curves for a variety of different conditions.

Introduction

Recovery percentages from oil reservoirs range from 5% for difficult oil to 50% for light oil in highly permeable sandstone reservoirs. Other reservoirs contain oil that is difficult to produce by conventional means, e.g., because the permeability is low, the reservoir is highly heterogeneous or the viscosity is high. A large area of application of air injection lies in the recovery of medium viscosity, i.e., oil with a viscosity in the range between 10^3 and 10^4 [cP] [1, 2, 10, 11, 30, 33, 34, 35]. In this case the oxygen in the air burns the heavier components of oil, generating a heat wave leading to cracking and vaporization of lighter components. Air injection has as advantage its ready availability at any location [47], but the disadvantage that energy costs of compression can be considerable. The combustion process can also be considered for cleaning up soils [36].

Our interest is, however, in recovering low viscosity oil from low permeability heterogeneous reservoirs using air injection leading to oil combustion. There is a large body of literature describing the use of HPAI (high pressure air injection, starting at ∼100 bars) to recover oil from these reservoirs. HPAI was first introduced in 1979 in the Buffalo Field [15]. Air injection is very effective in heterogeneous permeable reservoirs as the oil evaporates in the lower permeable parts to be collected in the higher mobility streaks. The advantage of high pressures is the high solubility of the light components in the liquid oil, which is conducive to a higher oil recovery.

[*]Instituto Nacional de Matemática Pura e Aplicada, Rio de Janeiro, Brazil. E-mail: alexei@impa.br

[†]Corresponding author: TU Delft, Civil Engineering and Geosciences, Stevinweg 1, 2628 CE Delft, The Netherlands. E-mail: J.Bruining@tudelft.nl

[‡]Instituto Nacional de Matemática Pura e Aplicada, Rio de Janeiro, Brazil. E-mail: marchesi@impa.br

However, the disadvantage of HPAI is that its application is confined to reservoirs at large depths. At shallower depths, an alternative is to inject air at medium pressures (∼10-90 bars) for light oil in heterogeneous low permeability reservoirs. The question is whether acceptable recovery efficiencies can also be attained at medium pressures. Indeed, compared to HPAI, there is less dissolution of the light components at medium pressures, thus reducing the displacement efficiency. De Zwart et al. [13] compare equation of state (EOS) models with multi-component combustion models to assess their applicability to in-situ combustion for HPAI conditions. Even for HPAI, De Zwart et al. conclude that air injection cannot be modeled as a flue gas displacement process as it results in an underestimate of the recovery because the stripping and condensation mechanisms are not adequately captured [39]. This means that stripping and condensation play an important role also at medium pressures; this is a result of the present paper.

There is literature that deals directly or indirectly with medium pressure air injection. This process has been studied experimentally, but no dedicated modeling for this process has been formulated. As we will show, combustion at medium pressures is characterized by medium temperature oxidation (MTO). Greaves et al. [23] carried out two tests on a light Australian oil (38.8^o API), starting at initial residual oil saturation of $S_o = 0.41$ and 0.45, at an operating pressure of 70 bar and initial bed temperature of 63^oC. The combustion temperature was about 250^o C in both tests. High combustion front velocities were achieved in all tests, varying from 0.15 to 0.31 [m/hour]. Fuel consumption, air requirement and oxygen utilization were generally favorable. Gilman et al. [21, 20] show that for the deeply dipping Hackbarry reservoir air injection can increase the light oil recovery to economical significance. They distinguish between application at high and low pressures in the field trial. The low pressure trial is conducted between 20-40 bars. Unfortunately supporting tube tests were only reported at high pressures (230 bar). The paper reports two incidents of fire, one at the high pressure test and one as the low pressure test, both occurring in the injection well. Gutierrez et al. [25] describe a low pressure (14 bar) laboratory test on light oil, which gave rise to relatively high temperatures (478 ^{o}C). The combustion is characterized initially by oxygen addition reactions followed by scission reactions. The test served as a good example why sufficiently high oxygen injection rates are required to stimulate the scission reactions. The mechanism envisioned by the authors is very similar to the mechanisms we describe here. Germain and Geyelin [18] describe combustion tube tests with light oil in heterogeneous low permeable (1-100 mD) reservoirs, using pressures of 40-45 bars, leading to temperatures between 260^oC and 370^oC.

Combustion for light oil and for medium viscosity oil [1, 2, 8, 9, 10, 11, 30, 33, 34, 35, 49, 52] are described by different mechanisms. For medium viscosity oils, the oxygen in the air burns coke, generating a heat wave leading to cracking, coke formation and vaporization of lighter components.

For light oil combustion coke formation is usually disregarded, although it can occur [29]. For light oil, evaporation and condensation are just as important as the oxidation reaction. As opposed to heavy oil combustion, light oil combustion occurs usually at lower temperatures because the oil is only partially oxidized. When evaporation is small and all of the light oil is oxidized relatively high temperatures can still occur. It is the purpose of this work to quantify the amounts of oil that is evaporated and combusted for light oil and relate them to the temperature of the oxidation zone in a MTO process.

In summary we have high temperature oxidation (HTO) (see references above) when heat conducted out of the reaction zone converts the oil to coke before it is combusted, low temperature oxidation (LTO) when the oxygen is incorporated in the hydrocarbon molecules to form alcohols, aldehydes, acids or other oxygenated hydrocarbons [23], [22], [26], and medium temperature oxidation (MTO) [23], [24], [18] when the oxidation reaction leads to scission of the molecule and forms small reaction products such as water, CO or CO_2.

Numerical modeling of the combustion process is difficult due to the disparity in time and space scales at which processes occur, see, however, Gerritsen et al. [19]. Therefore it is essential to compare to models that allow analytical solutions. In this work we examine a very simplified

model for air injection in light oil reservoir leading to MTO. We consider only one component, e.g., heptane in dry porous rock to improve understanding of the oxidation/evaporation/condensation mechanism, which can be solved analytically. Heptane represents a single pseudo-component as liquid fuel, which is characterized by an average boiling temperature, density, viscosity etc. It turns out that the oxidation, evaporation and condensation often occur close to each other and move with the same speed in the porous medium. The temperature variation is bounded by the oil boiling temperature and, thus, not very large.

The presence of liquid fuel, which is mobile and can vaporize or condense is the main difficulty in the mathematical analysis we perform. We consider the problem in one-dimensional space, which allows analytical study. We expect that the one-dimensional problem contains many (though, of course, not all) properties of combustion in real-world three-dimensional systems. In particular, our study may contribute to understanding the processes of High Pressure Air Injection (HPAI) [39].

The mathematical theory of combustion in porous medium is well developed for immobile fuels, e.g., [6, 9, 38, 46, 49]. When the fuel is liquid and, additionally, undergoes gas-liquid phase transitions, the problem becomes more complicated. It was shown in [37] that, in the case of liquid fuel, the combustion wave has a resonant structure similar to that encountered earlier in detonation problems, see [16, 31, 48, 51] and also [27] for mathematical theory. In this case at some point (resonant point) in the internal structure of the wave, the Buckley-Leverett characteristic speed is equal to the combustion velocity. In this resonant case, analysis of the internal wave structure (the reaction zone) is necessary in order to obtain macroscopic parameters of the wave. However, the determining equations appear to be independent of the particular form of the rate expressions, as soon as one of the processes is much faster (in our applications, vaporization is usually much faster than combustion).

In this paper, we extend the model suggested in [37], including diffusive and capillary pressure effects and considering general values of physical parameters. The mathematical model is given by a system of multi-phase flow equations with additional terms describing reaction and vaporization rates, and an energy balance equation. When diffusive and capillary effects are neglected, we find a general solution, consisting of three nonlinear waves, which are the thermal, combustion and saturation waves. The main difficulty of the analysis is the study of combustion wave, which we call the MTO wave. In this wave all physical processes, reaction, vaporization, condensation and filtration, are active. The name of the wave comes from the fact that the maximum temperature is bounded by the liquid boiling temperature and, thus, cannot become very high. Finally, we analyze the effect of capillary effects and diffusive terms, and give bounds for macroscopic parameters of the wave.

The paper is organized as follows. Section 1 describes the physical model and presents the dimensionless equations. Section 2 describes wave sequence solutions. Section 3 studies the MTO wave profile. Section 4 presents a numerical example. Section 5 studies the efficiency of MTO as a recovery process, i.e., oil produced versus gas injected for realistic problem parameters. Section 6 sets bounds to the effect of diffusive processes. We end with some conclusions.

1 Model

We study two-phase flow possessing a combustion front when a gaseous oxidizer (air) is injected into porous rock filled with light oil. The temperature of the medium is bounded by the boiling point of the liquid and, thus, remains relatively low. In our applications we disregard gaseous phase reactions. Many references indicate that gas-phase reactions in in-situ combustion play a minor role [5] with respect to the reactions with liquid or solid fuel. However, these references also point out that gas phase reactions can be important for HPAI [4]. In view of the role played by free radicals [28, 32] in these reactions [45], characterizing the situations in which gas phase reactions

play a significant role is a matter of debate. There are numerous references that indicate that gas phase reactions in porous media in itself are important [3, 41, 44, 53]. When oxygen reacts with liquid hydrocarbons at low temperatures, a series of reactions may occur that convert hydrocarbons into oxygenated hydrocarbons (ketones, alcohols, aldehydes). Further oxidation leads to complete combustion of the oxygenated hydrocarbons; in this paper the combined reaction to oxygenated hydrocarbons and the subsequent reaction to gaseous products is simplified in the form of a single reaction modeled as

$$\nu_l(\text{hydrocarbons}) + \text{O}_2 \rightarrow \nu_g\,(\text{gaseous products}), \tag{1.1}$$

i.e., one mole of oxygen reacts with ν_l moles of initial (liquid) hydrocarbons generating ν_g moles of gaseous products (H_2O, CO_2, etc.). In this model, all hydrocarbons are grouped into a single pseudo-component, while the differences in physical properties (density, viscosity, boiling temperature, etc.) of the liquid due to changes of its composition are disregarded. This may not be appropriate for crude oil or if LTO occurs. We neglect water that may be present initially or that condenses from steam in the reaction products.

We study one-dimensional two-phase (liquid and gas) flow in the positive spatial direction x. The liquid has saturation s_l, describing the occupied fraction of pore volume. The saturation of gas is, therefore, equal to $s_g = 1 - s_l$. In the gaseous phase, we distinguish the molar fraction of the hydrocarbon Y_h and the molar fraction of oxygen Y_o. The remaining components with fraction $Y_r = 1 - Y_h - Y_o$ consist of reaction products and inert components of the injected gas. The molar densities are indicated by ρ. The molar mass balance equations for liquid and gas components are

$$\frac{\partial}{\partial t}\varphi\rho_l s_l + \frac{\partial}{\partial x}\rho_l u_l = -\nu_l W_r - W_v, \tag{1.2}$$

$$\frac{\partial}{\partial t}\varphi Y_h\rho_g s_g + \frac{\partial}{\partial x}\rho_g u_{gh} = W_v, \tag{1.3}$$

$$\frac{\partial}{\partial t}\varphi Y_o\rho_g s_g + \frac{\partial}{\partial x}\rho_g u_{go} = -W_r, \tag{1.4}$$

$$\frac{\partial}{\partial t}\varphi Y_r\rho_g s_g + \frac{\partial}{\partial x}\rho_g u_{gr} = \nu_g W_r. \tag{1.5}$$

The reaction W_r and vaporization W_v rates are defined in Eqs. (1.15) and (1.17) below. The important thing to know about the vaporization rate is that it is much larger than the reaction rate.

The liquid, gas and total Darcy velocities have the form

$$u_l = -\frac{k_l}{\mu_l}\frac{\partial P_l}{\partial x}, \quad u_g = -\frac{k_g}{\mu_g}\frac{\partial P_g}{\partial x}, \quad u = u_l + u_g. \tag{1.6}$$

with viscosities $\mu_l(T)$, $\mu_g(T)$, phase permeability functions $k_l(s_l)$, $k_g(s_g)$, and pressures P_l and P_g of the liquid (l) and gas (g). The capillary pressure is defined as

$$P_c(s_l) = P_g - P_l = \frac{\sigma\cos\Theta}{\sqrt{k/\varphi}}J(s_l), \tag{1.7}$$

where the factor multiplying the Leverett J-function is taken as a constant in our problem [7]. In this paper, we will only use the property $J'(s_l) \leq 0$. It is convenient to express the liquid and gas velocities as

$$u_l = uf_l + \frac{f_g k_l}{\mu_l}P_c'(s_l)\frac{\partial s_l}{\partial x}, \quad u_g = u - u_l, \tag{1.8}$$

where the prime denotes the derivative with respect to the function argument, and the liquid and gas fractional flow functions are

$$f_l(s_l, T) = \frac{k_l/\mu_l}{k_l/\mu_l + k_g/\mu_g}, \quad f_g = 1 - f_l. \tag{1.9}$$

The Darcy velocities for gas components in (1.3)–(1.5) are

$$u_{gj} = Y_j u_g - \varphi D s_g \frac{\partial Y_j}{\partial x} \qquad (j = h, o, r). \tag{1.10}$$

As a first approximation, we use the same diffusion coefficient D for all gas components (see, however, the Stefan–Maxwell relations in [7] for the full composition dependence). This is only strictly allowed under certain conditions that are pointed out in [43].

Taking the sum of (1.3)–(1.5) and using (1.10) with $Y_h + Y_o + Y_r = 1$ yields the equality $u_{gh} + u_{go} + u_{gr} = u_g$ as well as the balance law for the total gas as

$$\frac{\partial}{\partial t}\varphi \rho_g s_g + \frac{\partial}{\partial x}\rho_g u_g = (\nu_g - 1)W_r + W_v. \tag{1.11}$$

Assuming that the temperature of solid rock, liquid and gas are equal, we write the heat balance equation as

$$\frac{\partial}{\partial t}\left(C_m + \varphi c_l \rho_l s_l + \varphi c_g \rho_g s_g\right)\Delta T + \frac{\partial}{\partial x}(c_l \rho_l u_l + c_g \rho_g u_g)\Delta T = \lambda \frac{\partial^2 T}{\partial x^2} + Q_r W_r - Q_v W_v, \tag{1.12}$$

where $\Delta T = T - T^{ini}$ with initial reservoir temperature T^{ini}. In this equation, the heat capacities C_m, c_l, c_g are taken as constants, which is a good approximation and facilitates the analysis. We neglected heat losses, which are usually very small in field applications (however, taking into account heat losses becomes essential for interpreting laboratory experiments).

We use the ideal gas law to define

$$\rho_g = P_g/RT. \tag{1.13}$$

Pressure variations are assumed to be small compared to the prevailing pressure of gas, so we take $P_g \approx const$ in (1.13) and all other thermodynamic relationships. The liquid density ρ_l is assumed to be constant.

The partial pressure of the gaseous hydrocarbon in liquid-gas equilibrium can be approximated by the Clausius-Clapeyron relation written as

$$Y_h^{eq} P_g = P_{atm} \exp\left(-\frac{Q_v}{R}\left(\frac{1}{T} - \frac{1}{T^{bn}}\right)\right), \tag{1.14}$$

where T^{bn} is the (normal) liquid boiling point measured at atmospheric pressure P_{atm}. Taking $Y_h^{eq} = 1$ in (1.14), one recovers the actual boiling temperature $T = T^b$ at the gas pressure P_g. In our analysis, we will not use the particular form (1.14), but only rely on the fact that Y_h^{eq} increases with temperature and $Y_h^{eq} \to 1$ as $T \to T^b$, where T^b is the boiling point at the prevailing pressure. Even if there are better boiling point relations than Clausius-Clapeyron (see [42]), the relation (1.14) is sufficiently accurate for our purpose.

The vaporization rate in the two phase region is given by

$$W_v = -k_e\left(Y_h - Y_h^{eq}\right). \tag{1.15}$$

If k_e is large this approach describes the situation close to local thermodynamic equilibrium for the gaseous hydrocarbon mole fraction Y_h, i.e., instantaneous vaporization. In the absence of liquid,

clearly there is no vaporization, and condensation occurs when $Y_h > Y_h^{eq}$. Thus, the vaporization rate W_v vanishes under the conditions

$$W_v = 0 \qquad \text{when} \qquad s_l > 0,\ Y_h = Y_h^{eq} \quad \text{or} \quad s_l = 0,\ Y_h \le Y_h^{eq}. \tag{1.16}$$

For an reaction rate one usually employs a rate equation of the form

$$W_r = A_r \varphi \rho_l s_l \left(\frac{P_g Y_o}{P_{atm}}\right)^n \exp\left(-\frac{T^{ac}}{T}\right), \tag{1.17}$$

with the pre-exponential factor A_r and the activation temperature $T^{ac} = E_{ac}/R$. We use the empirical form of the reaction rate equation [14] because it allows us to obtain an analytical solution and these simplified reaction rate equations are also used in the engineering literature. There is an extensive literature on reaction rate equations and more realistic models may include pore diffusion [7, 32], specific surface areas that change with time and other mechanisms. However, inserting these complexities usually prevents finding an analytical solution. The analysis and results in the paper do not depend on the particular form of the reaction rate and Eq. (1.17) is only relevant for the detailed shape of the reaction zone.

1.1 Dimensionless equations

Dimensionless variables, reaction and vaporization rates are introduced as the ratios

$$\tilde{t} = \frac{t}{t^*}, \quad \tilde{x} = \frac{x}{x^*}, \quad \tilde{\theta} = \frac{T - T^{ini}}{\Delta T^*}, \quad \tilde{u} = \frac{u}{u^*}, \quad w_r = \frac{W_r}{W_r^*}, \quad w_v = \frac{W_v}{W_v^*}, \tag{1.18}$$

where the reference quantities denoted by an asterisk are

$$\begin{gathered} t^* = \frac{\varphi \rho_g^*}{W_r^*},\ x^* = \frac{\rho_g^* u^*}{W_r^*},\ \rho_g^* = \frac{P_g}{R T^{ini}},\ \Delta T^* = T^b - T^{ini}, \\ \mu_l^* = \mu_l(T^{ini}),\ W_r^* = A_r \varphi \rho_l \left(\frac{P_g}{P_{atm}}\right)^n \exp\left(-\frac{T^{ac}}{T^{ini}}\right),\ W_v^* = k_e. \end{gathered} \tag{1.19}$$

The reference value u^* is related to the Darcy injection velocity and will be specified later. The dimensionless quantities $\tilde{\theta}$ and $\tilde{u}$ describe the temperature distribution (measured from the reservoir condition) and Darcy velocity, respectively. The length scale x^* in (1.19) is the ratio between rate of oxygen injection and rate of oxygen consumption in the MTO reaction at initial temperature. It is a reference length of the MTO reaction region. Dimensionless parameters and the dimensionless capillary diffusion coefficient D_c are introduced as

$$\begin{gathered} \alpha_l = \frac{\varphi c_l \rho_l}{C_m},\ \alpha_g = \frac{\varphi c_g \rho_g^*}{C_m},\ \beta = \frac{\rho_g^*}{\rho_l},\ \varepsilon = \frac{W_r^*}{W_v^*}, \\ Pe_T = \frac{C_m x^* u^*}{\lambda},\ Pe = \frac{x^* u^*}{D},\ Pe_c = \frac{x^* u^* \mu_l^*}{\sigma \sqrt{k\varphi} \cos\Theta},\ D_c(\theta, s_l) = -\frac{k_l/\mu_l}{k/\mu_l^*} f_g J'(s_l), \\ q_v = \frac{\varphi \rho_g^* Q_v}{C_m \Delta T^*},\ q_r = \frac{\varphi \rho_g^* Q_r}{C_m \Delta T^*},\ \theta_h = \frac{Q_v}{R \Delta T^*},\ \theta_0 = \frac{T^{ini}}{\Delta T^*},\ \theta_{ac} = \frac{T^{ac}}{\Delta T^*}. \end{gathered} \tag{1.20}$$

Here Pe_T, Pe and Pe_c are Peclet numbers for thermal and molar mass diffusions and capillary pressure effects; q_v and q_r describe the vaporization and reaction heats relative to the heat accumulated in the rock, etc. Note that $D_c \ge 0$ since the Leverett J-function in (1.7) decreases with s_l.

The governing system consists of equations (1.12), (1.2), (1.11), (1.3), (1.4). To transform this system to dimensionless form, we use (1.8) for the Darcy velocities of liquid and total gas, (1.10) for the Darcy velocities of gas components, and dimensionless variables and parameters given in (1.18)–(1.20). This procedure yields (dropping tildes)

$$\frac{\partial}{\partial t}\left(1+\alpha_l s_l+\alpha_g S_g\right)\theta+\frac{\partial}{\partial x}\left(\alpha_l u_l+\alpha_g U_g\right)\theta = \frac{1}{Pe_T}\frac{\partial^2\theta}{\partial x^2}+q_r w_r-\frac{q_v w_v}{\varepsilon}, \tag{1.21}$$

$$\frac{\partial s_l}{\partial t}+\frac{\partial u_l}{\partial x} = -\nu_l\beta w_r-\frac{\beta w_v}{\varepsilon}, \tag{1.22}$$

$$\frac{\partial S_g}{\partial t}+\frac{\partial U_g}{\partial x} = (\nu_g-1)w_r+\frac{w_v}{\varepsilon}, \tag{1.23}$$

$$\frac{\partial}{\partial t}Y_h S_g+\frac{\partial}{\partial x}U_{gh} = \frac{w_v}{\varepsilon}, \tag{1.24}$$

$$\frac{\partial}{\partial t}Y_o S_g+\frac{\partial}{\partial x}U_{go} = -w_r. \tag{1.25}$$

This is a system of five equations for the variables θ, s_l, u, Y_h, Y_o dependent on t and x. The other quantities such as u_l, U_g, U_{gh}, etc. are dimensionless functions of the dependent variables $(\theta, s_l, u, Y_h, Y_o)$ and their derivatives specified as follows

$$u_l = u f_l-\frac{D_c}{Pe_c}\frac{\partial s_l}{\partial x}, \tag{1.26}$$

$$U_g = uF_g+\frac{D_c}{Pe_c(1+\theta/\theta_0)}\frac{\partial s_l}{\partial x}, \quad U_{gj} = U_g Y_j-\frac{s_g}{Pe(1+\theta/\theta_0)}\frac{\partial Y_j}{\partial x}, \qquad (j=h,o) \tag{1.27}$$

$$S_g(\theta, s_l) = \frac{1-s_l}{1+\theta/\theta_0}, \quad F_g = \frac{1-f_l}{1+\theta/\theta_0}. \tag{1.28}$$

Here the capital U, S and F are used to denote "temperature-corrected" quantities by a factor $(1+\theta/\theta_0)^{-1}$.

For the equilibrium fraction of hydrocarbons in the gaseous phase, we write (1.14) in dimensionless form as

$$Y_h^{eq}(\theta) = \exp\left(\frac{\theta_h}{\theta_0+1}-\frac{\theta_h}{\theta_0+\theta}\right). \tag{1.29}$$

Note that Y_h^{eq} increases with θ. The reaction rate (1.17) in dimensionless form is given by

$$w_r = s_l Y_o^n \exp\left(\frac{\theta_{ac}}{\theta_0}-\frac{\theta_{ac}}{\theta_0+\theta}\right). \tag{1.30}$$

Typical liquid and gas viscosities have the properties

$$\mu_l'(\theta) < 0, \quad \mu_g'(\theta) > 0. \tag{1.31}$$

The typical fractional flow function $f_l(s_l, \theta)$ defined in (1.9) is nonzero (positive) for $s_l^{irr} < s_l < 1$ with residual (irreducible) liquid concentration $s_l^{irr} > 0$. As a function of s_l, it has an S-shaped form with a single inflection point; also $f_l = \partial f_l/\partial s = 0$ for $s = s_l^{irr}$ and $f_l = 1$, $\partial f_l/\partial s = 0$ for $s = 1$, as shown in Fig. 1. It follows from (1.31) and (1.9) that

$$\frac{\partial f_l}{\partial \theta} \geq 0. \tag{1.32}$$

All parameters in (1.20) are assumed to be constant, except for $D_c(\theta, s_l)$. The assumption of fast vaporization rate as compared to oxidation rate can be expressed as $\varepsilon \ll 1$ (a typical value of ε can be 10^{-5}).

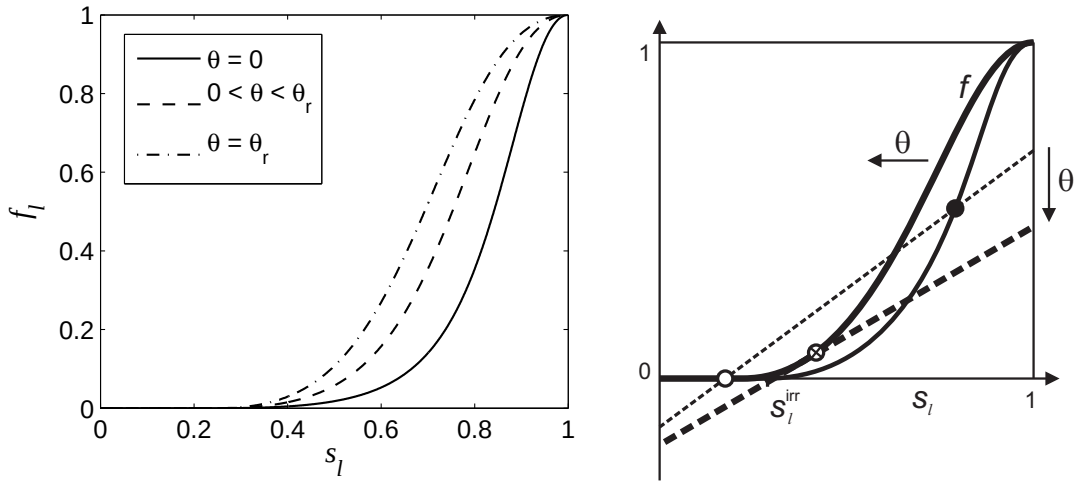

Figure 1: Left: Fractional flow function $f_l(s_l, \theta)$ for various values of $0 \leq \theta \leq \theta_r$ as described at the end of Section 1. For the definition of θ_r, see below. Right: The solid curves are the graph of the flow functions $f_l(s_l, \theta)$ with $\theta = \theta_r$ (bold curve) and $\theta < \theta_r$ (thin curve). As explained in Sections 2 and 3, the dashed lines represent schematically the s_l-dependence of the right-hand side of equation (2.24), (3.8) or (3.15). The value of the slope lies between 0 and 1, see (2.17); also the line intersects the negative part of the vertical axis. The two situations of interest are illustrated, viz. the line is tangent or has two intersection points. The tangency point (crossed dot) corresponds to the resonant state in the wave profile. In the reaction region (RR), the upper intersection (black dot) is relevant and it moves towards lower values of the saturation as the temperature increases. In the vaporization region (VR) the lower open circle is relevant and it moves to higher saturation values as the temperature increases. The only point that satisfies saturation continuity is the resonance point, indicated with a cross inside a circle. It occurs at θ_r, the highest temperature in the profile that corresponds to the boundary between the VR and RR.

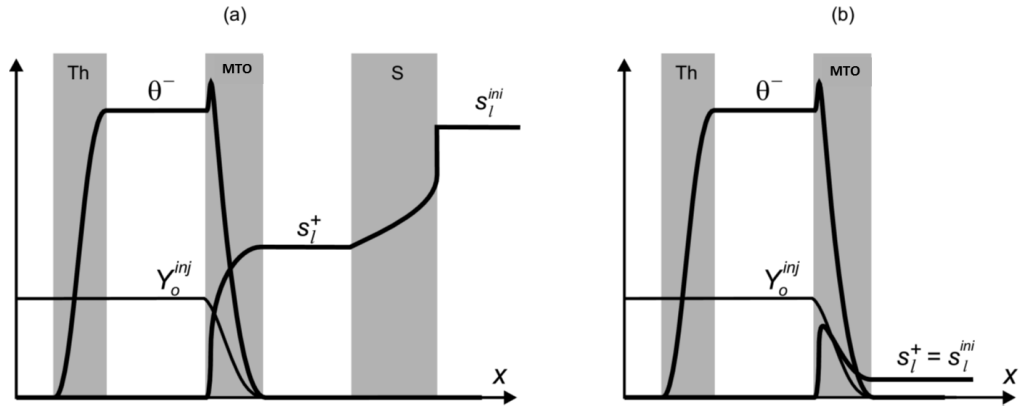

Figure 2: Wave sequence solutions with the thermal (Th), MTO and saturation (S) waves. Indicated are the distributions of the temperature θ, liquid saturation s_l and oxygen fraction Y_o. The MTO wave has (a) resonant and (b) non-resonant profile, see Section 3. The value of s_l^{ini} determines which of the cases occurs, (a) or (b).

2 Wave sequence solutions

Let us assume the initial reservoir conditions

$$t = 0,\ x \geq 0: \quad \theta = 0, \quad s_l = s_l^{ini}, \quad Y_h = Y_h^{eq}(0), \quad Y_o = 0, \tag{2.1}$$

corresponding to the reservoir containing oil and inert gas ($0 < s_l^{ini} < 1$) or liquid oil only ($s_l^{ini} = 1$). The injection conditions are

$$x = 0,\ t \geq 0: \quad \theta = s_l = Y_h = 0, \quad Y_o = Y_o^{inj}, \quad u = u^{inj}, \tag{2.2}$$

corresponding to the injection of oxidizer (air) at the reservoir temperature. It is assumed that there are no gaseous hydrocarbons in the injected gas, $Y_h = 0$.

For large times, we can look for a solution of system (1.21)–(1.25) with initial and boundary conditions (2.1), (2.2) as a sequence of waves separated by constant states. As we will see below, in this solution we have up to three (thermal, MTO and saturation) waves, Fig. 2.

2.1 Thermal wave

The thermal wave is the slowest wave due to high heat capacity of the rock, Fig. 2. Therefore, the thermal wave travels in the region of the reservoir where the liquid and gaseous hydrocarbons were swept by the MTO wave, i.e., $s_l = 0$. Also, $Y_h = 0$, as the injected gas contains no gaseous hydrocarbons. Hence, $f_l = w_r = w_v = 0$. Since there is no reaction, we have constant oxygen fraction $Y_o = Y_o^{inj}$. The temperature in the thermal wave changes from $\theta = 0$ upstream, the same as at the injection point (2.2), to some value θ^- downstream. The Darcy velocity upstream of the thermal wave is the injection Darcy velocity $u = u_{inj}$ according to (2.2).

In the region with no liquid, equation (1.21) becomes

$$\frac{\partial}{\partial t}(1 + \alpha_g S_g)\theta + \frac{\partial}{\partial x}\alpha_g U_g \theta = \frac{1}{Pe_T}\frac{\partial^2 \theta}{\partial x^2}. \tag{2.3}$$

The temperature-corrected gas Darcy velocity U_g is described by (1.23) with $w_r = w_v = 0$. From this equation, we have the variation $\delta U_g \sim \delta S_g(\delta x/\delta t)$ in absolute value. Under the assumption (confirmed later) that the thermal wave is slow, i.e., $\delta x/\delta t \ll 1$, we have $\delta U_g \ll 1$. Therefore, U_g is approximately constant

$$U_g = \frac{u}{1 + \theta/\theta_0} \approx u^{inj}, \tag{2.4}$$

where we first expressed U_g from (1.27), (1.28) with $s_l = 0$ and $f_l = 0$, and then used conditions (2.2). This expression, written as

$$u = u^{inj}(1 + \theta/\theta_0) \,, \tag{2.5}$$

describes the change of gas Darcy velocity due to gas thermal expansion.

Using (2.4) and neglecting the very small term $\alpha_g S_g$, where $\alpha_g \ll 1$ is the ratio between the gas and rock heat capacities in (1.20), we transform (2.3) to

$$\frac{\partial \theta}{\partial t} + \alpha_g u^{inj} \frac{\partial \theta}{\partial x} = \frac{1}{Pe_T} \frac{\partial^2 \theta}{\partial x^2}. \tag{2.6}$$

This equation has a well-known solution (see, e.g., [9]) describing the thermal wave, which travels with speed $v_T = \alpha_g u^{inj}$ and expands proportionally to $\sqrt{t/Pe_T}$ due to heat conduction in the rock. Since $\alpha_g \ll 1$, the thermal wave speed v_T is small indeed.

2.2 Medium-temperature oxidation wave

The MTO wave represents the most interesting wave in our solution. We assume that it is a traveling wave with constant speed v and constant states in the up- and downstream regions. In this wave, all the dependent variables θ, s_l, u, Y_h, Y_o depend on a single traveling coordinate $\xi = x - vt$, so that the wave profile is stationary in the frame moving with speed v. We will use the solution of the traveling wave to relate quantities at the upstream side (θ^-, s_l^-, u^-, Y_h^-, Y_o^-) with those at the downstream side (θ^+, s_l^+, u^+, Y_h^+, Y_o^+). It turns out that also the wave speed v can be obtained from these quantities. The equations for the wave profile are obtained by replacing $\partial/\partial x$ by $d/d\xi$ and $\partial/\partial t$ by $-vd/d\xi$ in (1.21)–(1.25); see also [37] for similar derivations. This procedure yields

$$\frac{d}{d\xi}\left(-v + \alpha_l \psi_l + \alpha_g \Psi_g\right)\theta = \frac{1}{Pe_T}\frac{d^2\theta}{d\xi^2} + q_r w_r - \frac{q_v w_v}{\varepsilon}, \tag{2.7}$$

$$\frac{d\psi_l}{d\xi} = -\beta\nu_l w_r - \frac{\beta w_v}{\varepsilon}, \tag{2.8}$$

$$\frac{d\Psi_g}{d\xi} = (\nu_g - 1) w_r + \frac{w_v}{\varepsilon}, \tag{2.9}$$

$$\frac{d\Psi_{gh}}{d\xi} = \frac{w_v}{\varepsilon}, \tag{2.10}$$

$$\frac{d\Psi_{go}}{d\xi} = -w_r, \tag{2.11}$$

where we introduced the fluxes in the moving coordinate frame parameterized by ξ as

$$\psi_l = u_l - v s_l, \quad \Psi_g = U_g - v S_g, \quad \Psi_{gh} = U_{gh} - v Y_h S_g, \quad \Psi_{go} = U_{go} - v Y_o S_g \tag{2.12}$$

for the liquid phase, gas phase, gaseous hydrocarbons and oxygen components. These fluxes are very convenient for representing the equations in a compact form; note that they are just notations, not variables. Using w_v and w_r expressed from (2.10), (2.11), we can write (2.7)–(2.9) in the form of derivatives with respect to ξ,

$$\frac{d}{d\xi}\left[\left(-v + \alpha_l \psi_l + \alpha_g \Psi_g\right)\theta + q_r \Psi_{go} + q_v \Psi_{gh}\right] = \frac{1}{Pe_T}\frac{d^2\theta}{d\xi^2}, \tag{2.13}$$

$$\frac{d}{d\xi}\left(\psi_l - \beta\nu_l \Psi_{go} + \beta \Psi_{gh}\right) = 0, \tag{2.14}$$

$$\frac{d}{d\xi}\left(\Psi_g + (\nu_g - 1)\Psi_{go} - \Psi_{gh}\right) = 0. \tag{2.15}$$

Adding ψ_l and $\Psi_g(1+\theta/\theta_0)$ from the first two equations in (2.12) and using the definitions in Eqs. (1.28) one finds

$$u = v + \Psi_g(1+\theta/\theta_0) + \psi_l. \tag{2.16}$$

This equation can be considered as an overall molar mass balance.

Note that, for positive wave speed v and fluxes Ψ_g and ψ_l, we have

$$0 < v < u. \tag{2.17}$$

In the absence of thermal and molar mass diffusion as well as of capillary forces, the derivative terms in (1.26), (1.27) vanish, and (2.12) takes the form

$$\psi_l = uf_l - vs_l, \quad \Psi_g = uF_g - vS_g, \quad \Psi_{gh} = Y_h\Psi_g, \quad \Psi_{go} = Y_o\Psi_g. \tag{2.18}$$

In particular, derivative terms vanish at the limiting states far upstream and far downstream of the MTO wave. Therefore, expressions (2.18) hold at these states.

The region upstream of the MTO wave contains injected gas with oxygen fraction $Y_o^{inj} > 0$ and no gaseous hydrocarbons, $Y_h = 0$, see (2.2). Since the reaction rate w_r must vanish at this limiting state, we are led to the condition $s_l = 0$ (no fuel), see (1.17). Note that all dimensionless parameters in (1.20), except for the Peclet numbers Pe_T, Pe, Pe_c, are independent of the reference speed u^*. Since we are free to choose u^*, it is convenient to specify it such that $\Psi_g = 1$ at the upstream limiting state; we will provide the value of u^* later in (2.30). The oxygen fraction Y_o^{inj} does not change in the thermal wave. Therefore, the oxygen flux in (2.18) is $\Psi_{go} = Y_o^{inj}\Psi_g = Y_o^{inj}$. In summary, the upstream $(-)$ state in the MTO wave satisfies the conditions

$$\xi \to -\infty: \quad s_l^- = \psi_l^- = 0, \quad \Psi_g^- = 1, \quad Y_h^- = \Psi_{gh}^- = 0, \quad Y_o^- = \Psi_{go}^- = Y_o^{inj}. \tag{2.19}$$

The temperature and Darcy velocity at the upstream state denoted by θ^- and u^- are unknown.

Downstream of the MTO wave there are liquid hydrocarbons with saturation $s_l^+ > 0$ and temperature $\theta = 0$. The equilibrium conditions $w_r = w_v = 0$ require $Y_o = 0$ and $Y_h = Y_h^{eq}(0)$, see (1.16), (1.17). For $Y_o = 0$, (2.18) yields $\Psi_{go} = 0$. Thus, we have the downstream $(+)$ state satisfies the conditions

$$\xi \to +\infty: \quad \theta^+ = 0, \quad Y_h^+ = Y_h^{eq}(0), \quad Y_o^+ = \Psi_{go}^+ = 0. \tag{2.20}$$

Of course, derivatives of all functions with respect to ξ vanish as $\xi \to \pm\infty$. The five unknown quantities in the limiting states are θ^-, s_l^+, the Darcy velocities u^-, u^+ and the wave speed v.

Three algebraic equations relating the limiting states of the MTO wave are found by integrating equations (2.13)–(2.15) from $-\infty$ to $+\infty$ with conditions (2.19), (2.20) and $\partial\theta/\partial\xi = 0$, i.e.,

$$q_v\Psi_{gh}^+ = (-v+\alpha_g)\theta^- + q_rY_o^{inj}, \tag{2.21}$$

$$\psi_l^+ + \beta\Psi_{gh}^+ = -\beta\nu_lY_o^{inj}, \tag{2.22}$$

$$\Psi_g^+ - \Psi_{gh}^+ = 1 + (\nu_g - 1)Y_o^{inj}, \tag{2.23}$$

where the left and right-hand sides correspond to the downstream $(+)$ and upstream $(-)$ limiting states, respectively. Using (2.18) with (2.20) for ψ_l^+ and Ψ_{gh}^+, equations (2.22), (2.23), (2.21) are written as

$$f_l(s_l^+, 0) = \frac{vs_l^+}{u^+} - \frac{\beta Y_h^{eq}(0)\Psi_g^+ + \beta\nu_lY_o^{inj}}{u^+}, \tag{2.24}$$

$$\Psi_g^+ = \frac{1 + (\nu_g - 1)Y_o^{inj}}{1 - Y_h^{eq}(0)}, \tag{2.25}$$

$$\theta^- = \frac{q_rY_o^{inj} - q_vY_h^{eq}(0)\Psi_g^+}{v - \alpha_g}. \tag{2.26}$$

Formula (2.16) at the limiting states (2.19), (2.20) and ψ_l^+ from (2.22) yields two equations, one of which is independent,

$$u^- = v + 1 + \theta^-/\theta_0, \tag{2.27}$$

$$u^+ = v + (1 - \beta Y_h^{eq}(0))\Psi_g^+ - \beta\nu_l Y_o^{inj}. \tag{2.28}$$

It is convenient to note that if the wave speed v was given, expressions (2.25)–(2.28) determine the values of θ^-, u^- and u^+. The remaining unknown s_l^+ is determined implicitly by equation (2.24), in a way reminiscent of the fractional flow method. The graphs of the left and right-hand sides of this equation as functions of s_l^+ are shown by the solid curve and the dashed line in Fig. 1. The intersection of these graphs gives the values of s_l^+. At least one intersection must exist, which represents the limiting state of the traveling wave. Generally there are two intersection points except for the degenerate case when the dashed line is tangent to the curve. Concentrating on the generic situation from now on, we will assume that there are two intersection points (the black and white dots in Fig. 1).

The condition $\Psi_g^- = 1$ in (2.19) determines the dimensional reference speed u^* as follows. Using (2.5) evaluated at the constant state θ^- and u^- from (2.27), we find

$$u^{inj} = 1 + v/(1 + \theta^-/\theta_0). \tag{2.29}$$

The dimensional form of this expression is

$$u^*\,[\mathrm{m/s}] = \frac{u^{inj}\,[\mathrm{m/s}]}{1 + v/(1 + \theta^-/\theta_0)}, \tag{2.30}$$

where we used the relation $\tilde{u} = u/u^*$ from (1.18) for u^{inj}, and the dimensional quantities are explicitly indicated. The velocity v needs still to be determined.

2.3 Saturation wave

The saturation wave can travel in the region downstream of the MTO wave, Fig. 2(a). In this region, the temperature is constant, $\theta = 0$. Thus, we have liquid-gas equilibrium $Y_h = Y_h^{eq}(0)$, so that there is neither vaporization nor condensation, see (1.16). The oxygen has been consumed completely in the MTO wave. Therefore, we have $Y_o = 0$ and no reaction occurs, see (1.17). Since the volume of each phase remains constant, the total Darcy velocity is also constant. It is equal to $u = u^+$ from (2.28), which corresponds to the downstream constant state of the MTO wave. Then equation (1.22) becomes

$$\frac{\partial s_l}{\partial t} + \frac{\partial u_l}{\partial x} = 0. \tag{2.31}$$

Considering large time and spatial scales, we can neglect the capillary term in (1.26) and write

$$u_l(s_l) = u^+ f_l(s_l, 0). \tag{2.32}$$

This equation has a self-similar solution (saturation wave) of the form $s_l = s_l(\zeta)$ with $\zeta = x/t$, where s_l changes from s_l^+ to s_l^{ini} with increasing ζ. This is a Buckley–Leverett solution constructed using the standard procedure involving the Welge tangent construction [50]. Briefly, it represents shock or rarefaction waves, possibly combined, see also [40]. Examples of such constructions are shown in Fig. 3. Note that the slope ζ^+ does not exceed the slope of the graph du_l/ds_l at the point $s_l = s_l^+$ and using (2.32), we write this observation as

$$\zeta^+ \le u^+ \frac{\partial f_l}{\partial s_l}(0, s_l^+). \tag{2.33}$$

One can check that the equality sign in (2.33) corresponds to $s_l^+ < s_l^{ini}$ and the inequality to $s_l^+ > s_l^{ini}$, see Fig. 3.

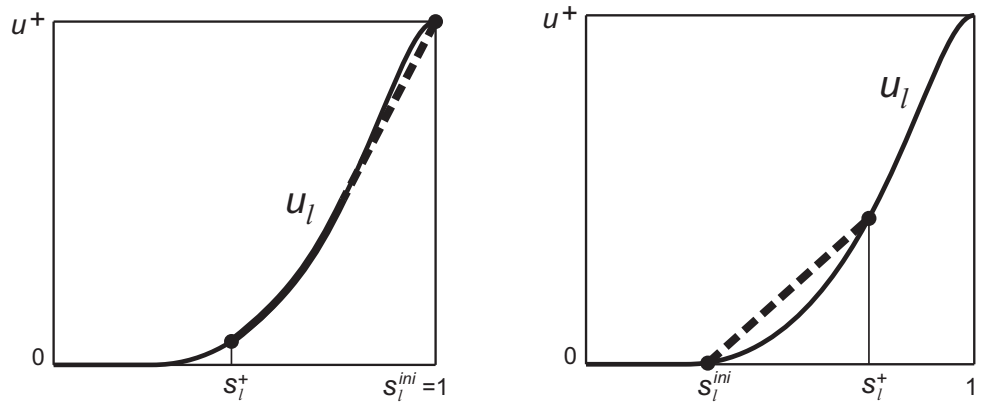

Figure 3: Construction of the saturation wave solution for the initial condition $s_l^{ini} = 1$ (left) and $s_l^+ > s_l^{ini}$ (right). Here we use the fractional flow function $f_l(s_l, \theta = 0)$, with boundary condition $s_l = s_l^+$. The bold curve denotes the rarefaction and the dashed lines denote the shock waves. The left figure demonstrates a combination of the rarefaction and shock waves.

2.4 Possible wave sequences

As we showed above, the (+) state of the MTO wave is determined by equation (2.24). This equation may have two solutions corresponding to the upper or lower intersection in Fig. 1, where the f_l-curve and the dashed line with slope v/u^+ correspond to the left- and right-hand sides of (2.24). Therefore, we have $v > u^+ \partial f_l/\partial s_l$ for the lower and $v < u^+ \partial f_l/\partial s_l$ for the upper choice of s_l^+. The MTO wave speed v must be smaller than the lowest speed in the saturation wave, $x/t = \zeta^+ \leq u^+ \partial f_l/\partial s_l$, where we used (2.33). This is only possible if the upper intersection in Fig. 1 is chosen for s_l^+.

We see that two types of wave sequence solutions are possible. The first solution shown schematically in Fig. 2(a) consists of the thermal, MTO and saturation waves separated by regions with constant states, and corresponds to the choice of the upper intersection in Fig. 1 for s_l^+. The second solution in Fig. 2(b) consists of the thermal and MTO waves, and corresponds to the choice of the lower intersection in Fig. 1 for s_l^+. Numerical computations in Section 4 show that the second type of solution exists only for very small values of the liquid saturation s_l^{ini} in the initial reservoir. Thus, only the solution with the saturation wave in Fig. 2(a) is of practical importance.

3 MTO wave profile

The MTO wave speed v, which was not determined so far, is found from the analysis of the wave profile. In this section, we neglect thermal and molar mass diffusion and capillary effects, i.e.,

$$\frac{1}{Pe_T} \approx 0, \quad \frac{1}{Pe} \approx 0, \quad \frac{1}{Pe_c} \approx 0. \tag{3.1}$$

Note that the Peclet numbers Pe_T, Pe, Pe_c defined in (1.20) are proportional to $x^* u^* \sim (u^*)^2$, see (1.19). Therefore, these parameters get large with increasing injection speed.

With (3.1), expressions (2.18) and (2.16) are valid at all points of the wave profile. Algebraic equations for the wave profile can be found by integrating equations (2.13)–(2.15) from $-\infty$ to ξ_1 as opposed to the derivation of Eqs. (2.21)–(2.23), where we integrated between $-\infty$ to ∞. Here

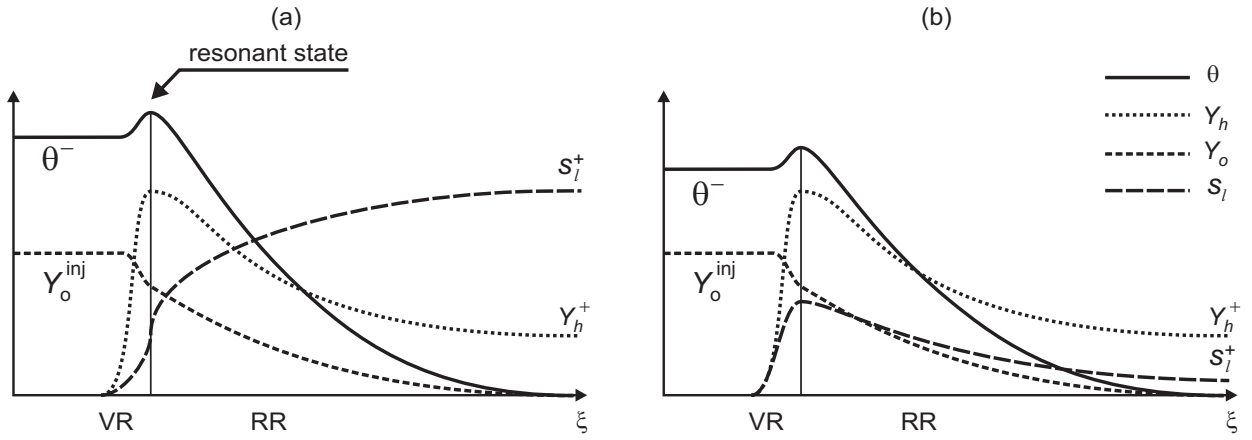

Figure 4: Schematic graphs of the (a) resonant and (b) non-resonant MTO wave profiles. Indicated are changes in the temperature θ, liquid oil saturation s_l, oxygen fraction Y_o and hydrocarbons fraction Y_h in the gas. The thin region VR is dominated by vaporization and the much wider region RR is dominated by MTO reaction (with slow condensation). In the case (a), VR and RR are joined by the resonance state. The VR is much thinner than the RR, with the ratio of order ε.

ξ_1 denotes any point along the wave. This yields

$$(-v+\alpha_l\psi_l+\alpha_g\Psi_g)\theta+q_r\Psi_{go}+q_v\Psi_{gh} = (-v+\alpha_g)\theta^-+q_rY_o^{inj}, \tag{3.2}$$

$$\psi_l-\beta\nu_l\Psi_{go}+\beta\Psi_{gh} = -\beta\nu_lY_o^{inj}, \tag{3.3}$$

$$\Psi_g+(\nu_g-1)\Psi_{go}-\Psi_{gh} = 1+(\nu_g-1)Y_o^{inj}, \tag{3.4}$$

where the constants on the right-hand sides are determined using conditions (2.19) at the limiting $(-)$ state, as already done for (2.21)–(2.23). Substituting ψ_l expressed in (3.3) into (3.2) and (2.16) yields

$$(-v-\alpha_l\beta\nu_l(Y_o^{inj}-\Psi_{go})-\alpha_l\beta\Psi_{gh}+\alpha_g\Psi_g)\theta+q_r\Psi_{go}+q_v\Psi_{gh} = (-v+\alpha_g)\theta^-+q_rY_o^{inj}, \tag{3.5}$$

$$u = v+\Psi_g(1+\theta/\theta_0)-\beta\nu_l(Y_o^{inj}-\Psi_{go})-\beta\Psi_{gh}. \tag{3.6}$$

Below we will use Eqs. (3.3)–(3.6).

3.1 Resonant wave profile

This section considers Figure 4a. First, let us consider the choice of the upper intersection (black dot) for s_l^+ in Fig. 1. We will prove below that for this choice the MTO wave speed v is determined by the internal (resonant) state of the wave profile, i.e., the point of tangency in Fig. 1. Our analysis is simplified in an essential way by the physical assumption that the vaporization rate is much faster than the reaction rate, $\varepsilon \ll 1$. Under this assumption we can divide the wave profile into the vaporization (VR) and reaction regions (RR), see Fig. 4. The vaporization region is very thin. Its width is approximately proportional to the ratio between the reaction and vaporization rates, $\varepsilon \ll 1$.

The surprising feature of the MTO wave is that the thin vaporization region is located upstream of the reaction region. Here the fraction Y_h of gaseous hydrocarbons raises from $Y_h = 0$ in the injected gas to the equilibrium value $Y_h = Y_h^{eq}(\theta)$ at the downstream end of the VR. Since this region is very thin and the reaction rate is not large, the oxygen consumption is negligible and we can neglect the reaction process in the VR. Thus, the oxygen flux Ψ_{go} in (2.11) does not change along VR, and it is equal to $\Psi_{go} = Y_o^{inj}$ according to (2.19) and our choice of $\Psi_g = 1$ at the

injection side ($Y_o = \Psi_{go}/\Psi_g$). Using this fact and relations (2.18), we solve (3.4)–(3.6). Note that in Eq. (3.4), the terms containing $\nu_g - 1$ cancel. This yields

$$\text{VR:}\quad \begin{aligned} &Y_o = \frac{\Psi_{go}}{\Psi_g} = (1-Y_h)Y_o^{inj}, \quad \Psi_g = \frac{1}{1-Y_h}, \\ &\theta = \theta^- + \frac{q_v - \alpha_l\beta\theta^- + \alpha_g\theta^-}{v(1-Y_h) + \alpha_l\beta Y_h - \alpha_g}Y_h, \quad u = v + \beta + \frac{1+\theta/\theta_0 - \beta}{1-Y_h}, \end{aligned} \tag{3.7}$$

where $\Psi_{go} = Y_o^{inj}$ was used and also $\Psi_g = 1/(1-Y_h)$ was used in the other formulae in (3.7). Expressions (3.7) furnish the quantities Y_o, Ψ_g, θ and u in terms of Y_h. It is easy to see that Ψ_g and u increase with Y_h. The same is true for θ provided the constants α_g and $\alpha_l\beta$ are sufficiently small. Since α_g and $\alpha_l\beta$ are the ratios of gas and rock heat capacities according to (1.20), they are small indeed.

Using (3.7) and ψ_l from (2.18) in (3.3), we obtain

$$\text{VR}: \quad f_l(s_l,\theta) = \frac{vs_l}{u} - \frac{\beta Y_h}{(1-Y_h)u}. \tag{3.8}$$

The graphs of the left and right-hand sides of this equation as functions of s_l have the form shown by the solid curve and the dashed line in Fig. 1. The solution in the VR is determined by the lower intersection point, since $s_l = Y_h = 0$ at the $(-)$ state (2.19). With increase of θ, the f_l-curve moves upwards according to (1.32). On the contrary, (3.8) says that the dashed line moves down with simultaneous increases of Y_h and u. As a result, the value of s_l at the lower intersection point in Fig. 1 increases, and this increase is limited by the tangency point. The tangency point is determined using (3.8) by the condition

$$\frac{\partial f_l}{\partial s_l} = \frac{v}{u}, \tag{3.9}$$

where v/u is the slope of the dashed line in Fig. 1.

We showed that (3.7) and (3.8) determine the variables θ, s_l and u as increasing functions of Y_h, i.e., all of them increase in the downstream direction. With the increase of Y_h from zero, the maximum of s_l is attained at the tangency point (3.9). Further increase of Y_h in the VR is impossible.

Downstream of the VR, we have the reaction region (RR). In our model, RR is several orders of magnitude wider than the VR. In the RR, most of the MTO reaction occurs, as well as a slow condensation due to decrease of temperature along the gas flow. Along the RR, the equilibrium condition

$$\text{RR}: \qquad Y_h = Y_h^{eq}(\theta) \tag{3.10}$$

holds approximately. Because of the assumptions (3.1), we use ψ_l, Ψ_{gh} and Ψ_{go} from (2.18) and write equations (3.3)–(3.6) as

$$\text{RR:}\quad \begin{aligned} &f_l(s_l,\theta) = \frac{vs_l}{u} - \frac{\beta Y_h\Psi_g + \beta\nu_l(Y_o^{inj} - \Psi_{go})}{u}, \\ &\Psi_g = \frac{1 + (\nu_g - 1)(Y_o^{inj} - \Psi_{go})}{1-Y_h}, \\ &\theta = \frac{(v-\alpha_g)\theta^- - q_r(Y_o^{inj} - \Psi_{go}) + q_vY_h\Psi_g}{v + \alpha_l\beta\nu_l(Y_o^{inj} - \Psi_{go}) + \alpha_l\beta Y_h\Psi_g - \alpha_g\Psi_g}, \\ &u = v + \Psi_g(1 + \theta/\theta_0 - \beta Y_h) - \beta\nu_l(Y_o^{inj} - \Psi_{go}). \end{aligned} \tag{3.11}$$

We can also define the oxygen mole fraction as

$$Y_o = \frac{\Psi_{go}}{\Psi_g} = \frac{\Psi_{go}(1-Y_h)}{1+(\nu_g-1)(Y_o^{inj}-\Psi_{go})} \tag{3.12}$$

First, let us consider equations (3.11) in the simplified case when

$$\nu_g = 1, \quad \alpha_g = \alpha_l = q_v = \nu_l = 0, \tag{3.13}$$

which is a reasonable approximation, see numerical values in Tab. 1. Then equations (3.11)–(3.12) can be written as

$$\Psi_g = \frac{1}{1-Y_h}, \quad Y_o = \Psi_{go}(1-Y_h), \quad \theta = \frac{v\theta^- - q_r Y_o^{inj} + q_r \Psi_{go}}{v}, \quad u = v + \frac{1+\theta/\theta_0 - \beta Y_h}{1-Y_h}, \tag{3.14}$$

$$f_l(s_l,\theta) = \frac{vs_l}{u} - \frac{\beta Y_h}{(1-Y_h)u}. \tag{3.15}$$

One observes that Ψ_{go} given by (3.14) and $Y_h = Y_h^{eq}(\theta)$ given by (1.29) are increasing functions of θ. Similarly, using (3.14), one can check that Ψ_g, Y_o and u increase with Ψ_{go}. The oxygen flux Ψ_{go} decreases in the downstream direction, see (2.11) with positive w_r. The graphs of the left and right-hand sides of (3.15) in terms of s_l have the form shown by the solid curve and the dashed line in Fig. 1. Recall that we have chosen the upper intersection in Fig. 1 for s_l^+ at the downstream (+) state. The f_l-curve moves upward as θ increases, according to (1.32). On the contrary, the dashed line moves down with simultaneous increases of Y_h and u. As a result, the value of s_l at the upper intersection in Fig. 1 decreases as the temperature increases. This behavior is limited by the tangency point in Fig. 1 determined by condition (3.9). Indeed when the f_l curve increases too much no intersection point will occur.

In conclusion, the variables θ, u, Y_h, Y_o decrease in the flow direction in the RR, while s_l (determined by the upper intersection in Fig. 1) increases. The minimum value of s_l is attained at the tangency point (3.9), because as explained above the upper intersection point is chosen in the RR. The VR on the left and the RR on the right have to be connected. At the connection point all variables must have the same values. This is a fortiori true for the saturation. The continuity can only be obtained at resonance condition Eq. (3.9), which correspond to the tangent construction in Fig. 1. Note that $u\partial f_l/\partial s_l$ is the characteristic speed of the saturation wave for a given constant Darcy velocity u, see (2.31), (2.32). Therefore, (3.9) represents the resonance condition at the internal point of the wave profile, where the wave speed is equal to the characteristic speed of saturation wave.

As confirmed by numerical computations in Section 4, the form of the wave profile in the RR remains the same in the general case, i.e., the variables θ, u, Y_h, Y_o decrease along the gas flow in the RR, while s_l (determined by the upper intersection in Fig. 1) increases. Thus, as in the simplified case, the VR and RR join at the resonance state determined by condition (3.9).

The values of the variables θ, s_l, Ψ_g, Y_h, Y_o, u at the resonance state together with the wave speed v can be determined by solving the system of equations (3.7)–(3.10) numerically. This means that we replace the variables θ, s_l, Ψ_g, Y_h, Y_o, u by θ_r, s_{lr}, Ψ_{gr}, Y_{hr}, Y_{or}, u_r in these equations and solve, using θ^- from (2.26) and Eq. (2.25). It was proved in [37] that this system has a unique solution in the physical domain in the simplified case (3.13). We expect that the same is true in the general case.

In summary we have seven unknowns, i.e., θ_r, s_{lr}, Ψ_{gr}, Y_{hr}, Y_{or}, u_r and the wave speed v. Eq. (3.7) comprise four equations, but it introduces an additional auxiliary variable, θ^-. Eqs. (3.8)–(3.10) add three equations and one more equation is obtained from (2.26) using Eq. (2.25). So we have seven equations for seven unknowns. This can be solved by standard algebraic equation solvers. These values are necessary for the construction shown in Fig. 1.

The general procedure for determining the MTO wave parameters and profile is summarized as follows. First, one determines the wave speed v and dependent variables at the resonant state as described in the previous paragraph. For given v, the limiting states are determined as described in Section 2.2, see (2.19), (2.20) and (2.24)–(2.28). In the VR, the variables Y_o, θ, u as functions of Y_h are given by (3.7). Then s_l as a function of Y_h is found by solving (3.8), where the smaller of the two solutions must be chosen. In the RR, the variables θ, s_l, u, Y_h, Y_o as functions of Ψ_{go} are determined by solving numerically the system (3.10), (3.11). An example of such computations is presented in Section 4.

It is an important conclusion that the MTO wave speed and the limiting states in our solution appear to be independent of the form of vaporization and reaction rates. If the expression for the reaction rate is known, e.g. (1.30), one can determine the dependence $\Psi_{go}(\xi)$ by solving differential equation (2.11) numerically, where all variables are expressed in terms of Ψ_{go} as described in the previous paragraph, and the initial condition is taken at the resonance state.

3.2 Non-resonant wave profile

This section considers Figure 4b, corresponding to the other choice of the solution s_l^+ of equation (2.24), which corresponds to the lower intersection (white dot) in Fig. 1. As we showed in Section 2, a separate saturation wave downstream of the MTO wave does not exist in this case. Therefore, the value $s_l^+ = s_l^{ini}$ is the liquid oil saturation in the initial reservoir, which allows to get the wave speed directly as opposed to the procedure for the resonant wave. Using $s_l^+ = s_l^{ini}$ in (2.24) with u^+ expressed from (2.28), we find the wave speed as

$$v = \frac{\beta Y_h^{eq}(0)\Psi_g^+ + \beta\nu_l Y_o^{inj} + (\Psi_g^+ - \beta Y_h^{eq}(0)\Psi_g^+ - \beta\nu_l Y_o^{inj}) f_l(s_l^{ini}, 0)}{s_l^{ini} - f_l(s_l^{ini}, 0)}. \tag{3.16}$$

where Ψ_g^+ is given by (2.25).

There must exist a wave profile satisfying equations (2.10), (2.11) and (3.3)–(3.6) with v given by (3.16). As earlier, the wave profile can be divided into two regions, VR and RR described by the same equations (3.7), (3.8) and (3.10), (3.11) as for the resonant wave profile. Since the lower (white dot) intersection in Fig. 1 is taken at both $(-)$ and $(+)$ limiting states, the same choice must be made at other points of the wave profile. This profile is shown schematically in Fig. 4(b).

The point joining the VR and RR is determined by equations (3.7), (3.8) of the VR with the additional equilibrium condition (3.10). Since the lower intersection in Fig. 1 is chosen for the solution of (3.8), we have the condition

$$\frac{\partial f_l}{\partial s_l} < \frac{v}{u}, \tag{3.17}$$

where v/u is the slope of the dashed line in Fig. 1. For the simplified case (3.13), it was proved in [37] that condition (3.17) implies that the wave speed v given by (3.16) is larger than the wave speed in the resonant case characterized by condition (3.9).

Existence of the wave profile can be checked numerically. As shown in the next section, the profile exists only for very small values of the initial oil saturation s_l^{ini}.

4 Numerical example

Let us consider reservoir parameters values given in Tab. 1. These values correspond to heptane (C_7H_{16}) and decane ($C_{10}H_{22}$) as a hydrocarbon pseudo-component. Parameters of the MTO reaction rate (1.17) vary a lot depending on specific conditions, and availability of reaction rate data is limited. In Tab. 1 we used the MTO rate parameters compatible with experimental results in [17].

Q_c	=	406 kJ/mol	T^{ini}	=	330 K	λ	=	3 W/m K	α_l	=	0.2285
Q_v	=	31.8 kJ/mol	T^{bn}	=	371 (447) K	D	=	3.7×10^{-6} m^2/s	α_g	=	0.0121
R	=	8.314 J/mol K	T^{b}	=	475 K	F_c	=	1.8×10^{-8} N	β	=	0.0531
C_m	=	2 MJ/m^{3}K	T^{ac}	=	7066 K	A_r	=	4060 1/s	q_v	=	0.0118
c_g	=	29 J/mol K	P_g	=	10^6 Pa	ν_l	=	0.090 (0.065) [mol/mol]	q_r	=	0.1503
c_l	=	224 (315) J/mol K	φ	=	0.3	ν_g	=	1.36 [mol/mol]	θ_h	=	26.136
ρ_l	=	6826 (5130) mol/m^3	Y_{inj}	=	0.21	n	=	0.5	θ_0	=	2.2754

Table 1: Values of dimensional and dimensionless reservoir parameters for heptane (decane). We use $F_c = \sigma\sqrt{k\varphi}\cos\Theta$ to denote the capillary force.

In our solutions, the wave speed and limiting states are fortunately independent of the elusive kinetic parameters. We use Sutherland's formula for the gas (air) viscosity and the Arrhenius model for the liquid viscosity [42] as (for T in Kelvin)

$$\begin{aligned} \text{Air:}\quad & \mu_g = \frac{7.5}{T+120}\left(\frac{T}{291}\right)^{3/2}\ (\text{cP}),\\ \text{Heptane:}\quad & \mu_l = 1.32\times 10^{-2}\exp\left(\frac{1006}{T}\right)\ (\text{cP}),\\ \text{Decane:}\quad & \mu_l = 1.423\times 10^{-2}\exp\left(\frac{1225}{T}\right)\ (\text{cP}). \end{aligned} \tag{4.1}$$

The relative permeability functions are taken as $k_l = (s_l - 0.25)^2$ for $s_l \geq 0.25$ (vanishing for $s_l \leq 0.25$) and $k_g = (1 - s_l)^2$.

First, consider the MTO wave with the resonant profile. The results are obtained for heptane in Fig. 5 and for decane in Fig. 6. The thick lines in the left picture of Figs. 5 and 6 show results of numerical computations for different values of the prevailing gas pressure P_g. Note that some of the dimensionless parameters in the last column of Tab. 1 change when the pressure P_g is changed. The dimensionless wave speed v and the variables θ, s_l, Ψ_g, Y_h, Y_o, u at the resonant state joining the VR and RR are found by solving numerically equations (3.7)–(3.10), where θ^- is expressed from (2.25), (2.26). The quantities θ^-, u^-, s_l^+, u^+ at the limiting states are found from (2.24)–(2.28), and the dimensionless u^{inj} is given by (2.29). The dimensional quantities in Figs. 5 and 6 are determined using (1.18), (1.19) and (2.30). We see that the downstream liquid saturation stays around the value $s_l^+ \approx 0.6$ for a large interval of pressures. Increase of the pressure leads to increase of temperatures and of the MTO wave speed relative to the injection speed. The right pictures in Figs. 5 and 6 show the maximum temperature and the boiling temperature as a function of pressure. We found that the simplified model parameters (3.13) yield similar results with a difference of about 20%.

The MTO wave profile consists of vaporization and reaction regions, see Fig. 4. We consider the VR as a very thin region in the upstream part of the profile, where the dependent variables change from the values at the $(-)$ limiting state to their values at the resonant state. In the RR, we can express θ, s_l, Ψ_g, Y_o, Y_h and u in terms of the oxygen flux Ψ_{go} by solving system (3.10), (3.11) numerically. Then the value of Ψ_{go} as a function of the moving coordinate in the flow direction ξ is given by solving the differential equation (2.11). The dimensional quantities can be found using (1.18), (1.19) and (2.30).

The results of such computations for the data in Tab. 1 are presented in Fig. 7. Here the VR is a very thin region between the constant $(-)$ state and the resonance state. On the right of the peak, we have the RR. In the RR, the wave profile is characterized by steep changes of all variables at higher temperatures, followed by slower variations at lower temperatures. Note also that the temperature θ attains a maximum at the resonance state. At this state, the MTO reaction in the

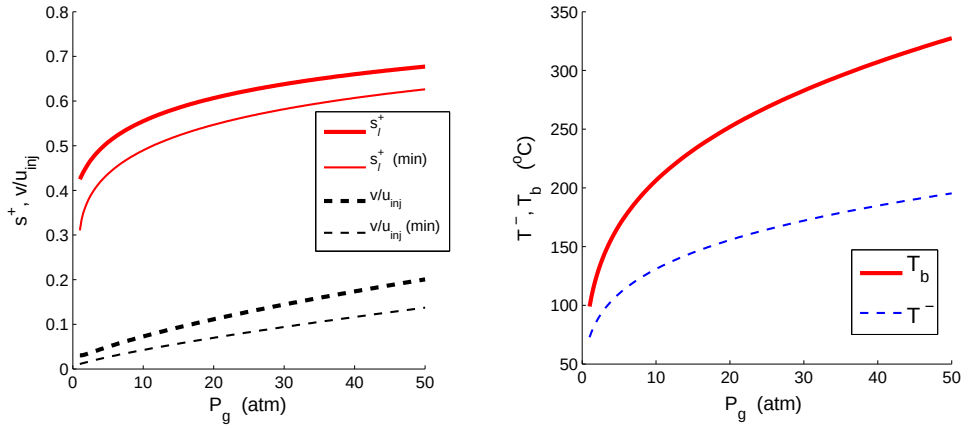

Figure 5: Dependence of parameters of the MTO wave for heptane with resonant profile on the gas pressure P_g (atm). Shown are the liquid saturation s_l^+ at the downstream (+) state and the ratio v/u^{inj} of the MTO wave speed and the Darcy velocity of injected gas (left). Thick lines correspond to the case of no diffusion and no capillary forces; thin lines indicate the lower bounds (minimal values) of s_l^+ and v/u^{inj} when capillary forces are taken into account. The boiling temperature T^b (°C) and the temperature T^- (°C) at the upstream (−) state are shown on the right.

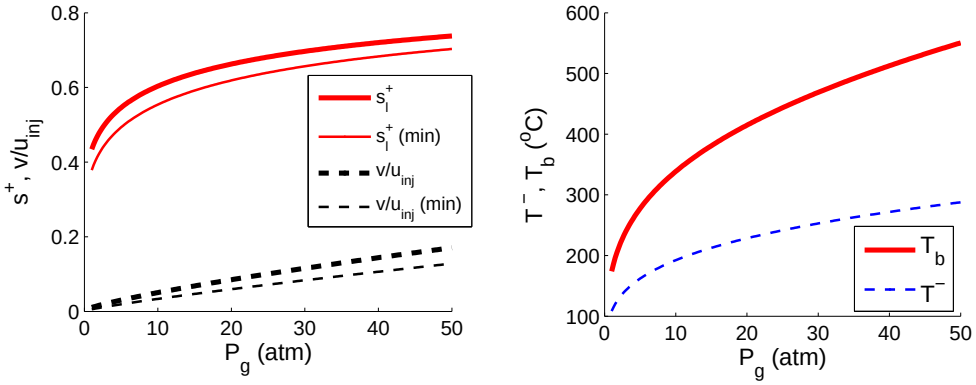

Figure 6: Dependence of parameters of the MTO wave for decane with resonant profile on the gas pressure P_g (atm). Shown are the liquid saturation s_l^+ at the downstream (+) state and the ratio v/u^{inj} of the MTO wave speed and the Darcy velocity of injected gas (left). Thick lines correspond to the case of no diffusion and no capillary forces; thin lines indicate the lower bounds (minimal values) of s_l^+ and v/u^{inj} when capillary forces are taken into account. The boiling temperature T^b (°C) and the temperature T^- (°C) at the upstream (−) state are shown on the right.

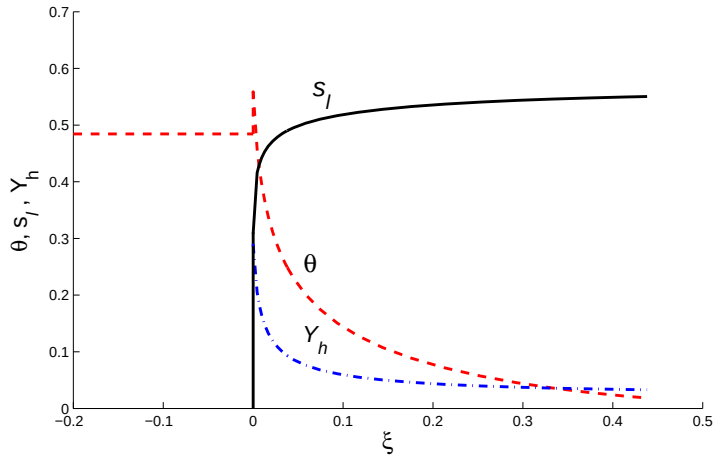

Figure 7: The MTO wave profile for parameters in Tab. 1 (heptane). Shown are the dimensionless variables θ, s_l and Y_h as functions of ξ (the dimensional length scale is $x^* = 19.1\,\mathrm{m}$). The thin VR appears as a peak, see also Fig. 4.

RR zone downstream is replaced by heat-consuming vaporization upstream, and this results in a sharp spike of $\theta(\xi)$.

For the initial reservoir and injection conditions (2.1), (2.2), the wave sequence solution consists of the thermal, MTO and saturation waves, see Fig. 2(a). In the case $s_l^{ini} = 1$ (initial reservoir filled by the oil), the saturation wave is the combination of a rarefaction and a shock wave, see also Fig. 3(a).

Finally, let us consider MTO waves with non-resonant profiles. These waves have speeds v higher than the resonant wave speed. Numerical computations show that, for such speeds, the lower intersection (white dot) in Fig. 1 lies in the region of connate liquid, where the fractional flow function f_l vanishes. Taking $f_l(s_l^{ini}, 0) = 0$ in equation (3.16) yields

$$s_l^{ini} = (\beta Y_h^{eq}(0)\Psi_g^+ + \beta\nu_l Y_o^{inj})/v. \tag{4.2}$$

Using the data in Tab. 1, formulae (1.29), (2.25) and the resonant wave speed $v = 0.0775$, we estimate

$$s_l^{ini} \sim 0.036. \tag{4.3}$$

We see that the MTO wave with non-resonant profile exists only when the initial reservoir contains oil of extremely low concentration. Therefore, in practical applications, the non-resonant MTO wave will be outside the scope of practical interest.

We see that the maximum temperature in the wave is roughly half of the boiling temperature (evaluated relative to the initial reservoir temperature), see Figs. 5 and 6. Computations show that this ratio is valid for liquid fuels with higher viscosity and boiling temperature. Recall that our model (with no thermal and molar mass diffusion and no capillary forces) was allowed only for wide reaction zones with slow reaction rates. Thus, such a simplified model is not valid for high pressures (e.g., in HPAI) when the temperature increases substantially. We conclude that the MTO wave solution just described is valid for liquids with typical boiling temperatures of light oil, e.g., heptane or decane, and moderate pressures. In section 6, we address the opposite case of high temperatures in the MTO wave.

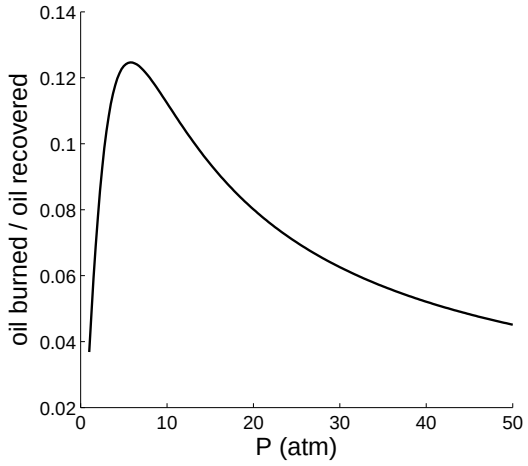

Figure 8: Dependence of the burned to recovered oil ratio for heptane depending on the gas pressure P_g (atm).

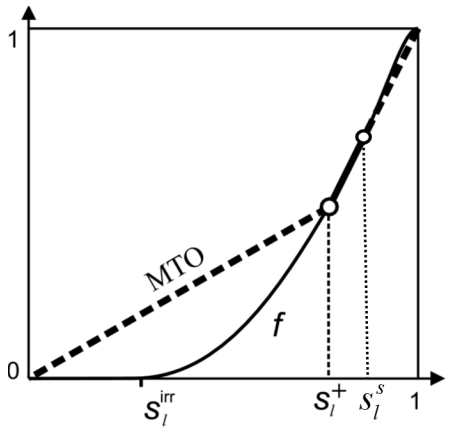

Figure 9: The plot of the flow function $f_l(s_l, \theta = 0)$. The computed value s_l^+ is used as a point in the fractional flow function that allows to obtain the saturation profile. From downstream to upstream the solution follows $f_l(s_l, \theta = 0)$ and consists of a shock from $s_l = 1$ to the shock saturation $s_l = s_l^s$, followed by a rarefaction and a shock from s_l^+ to $s_l = 0$ (see Fig. 2a).

5 Efficiency of MTO recovery

The amount of oil burned in the MTO wave relative to the amount of oil recovered in front of the MTO wave is computed as follows. The amount of burned oil is equal to $\nu_l \beta \Psi_{go}^-$. This follows from the fact that the injected oxygen flux Ψ_{go}^- is proportional to the amount of fuel burned. The amount of recovered liquid oil downstream of the MTO wave is given by the Darcy velocity $u_l^+ = u^+ f_l^+$, which can be computed by formulas (2.28), (2.24), and (2.25). Taking into account gaseous oil as the recovered one, we add βU_{gh}^+ in the denominator, and obtain

$$\frac{\text{burned oil}}{\text{recovered oil}} = \frac{\nu_l \beta \Psi_{go}^-}{u_l^+ + \beta U_{gh}^+}. \tag{5.1}$$

Computations of the ratio (5.1) for heptane are presented in Fig. 8. The amount of burned oil varies in the range of $5 \sim 12\%$.

Using the fractional flow function (see Dake [12] and Fig. 9) it turns out that there is a simple

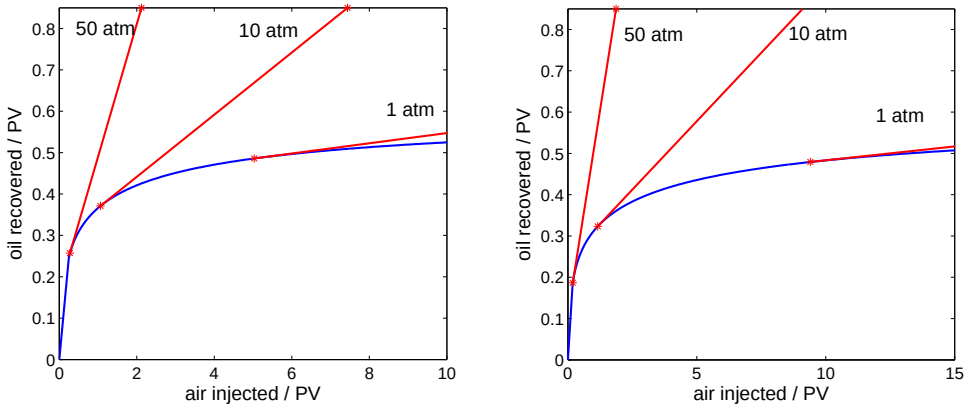

Figure 10: Pore volume (PV) of oil produced versus PV of air injected for heptane (left) and decane (right) combustion. The figures (left and right) are very similar albeit on a different scale.

graphical procedure that relates the pore volume of air injected to the pore volume of oil produced. The procedure, however, leads to the pore volume produced u^+ rather than the pore volume injected u^{inj}. As β is the ratio between gas density and liquid density it is usually small. Also the MTO wave velocity $v \ll 1$. Hence $u^+ \approx u^{inj} \approx 1$, see Eqs. (2.28) and (2.29).

The volume of oil produced versus the volume of gas injected is shown in Fig. 10 for different pressures, assuming that the initial oil saturation $s_l^{ini} = 0.85$. We observe that initially all curves show the same behavior. Then at $s_l = s_l^+$ the production rate continues as a straight line. The MTO wave is more effective for oil recovery at higher high pressures, as is shown in Fig. 10.

6 Effect of diffusive processes

Thermal and molar mass diffusion as well as capillary forces lead to diffusive processes and are important when steep changes occur in the dependent variables in the wave profile. As we saw in Sections 3 and 4, this is the case in the thin VR and, possibly, in the upstream part of the RR, where the MTO reaction is fast due to high temperatures. As a result, we can expect quantitative changes in the wave profile. For example, the spike in the temperature profile in Fig. 7 must widen and flatten due to the thermal diffusion. The importance of the diffusion and capillary forces may be very roughly estimated by using Peclet numbers Pe_T, Pe and Pe_c defined in (1.20). The effect is stronger for smaller Peclet numbers, i.e., for smaller injection velocities, since Pe_T, Pe and Pe_c are proportional to $x^*u^* \sim (u^*)^2$, see (1.19).

Finding the MTO wave profile in the general case is a nontrivial numerical problem. However, some useful quantitative information can be recovered. The only quantity we need to determine is the MTO wave speed v. Then the limiting states of the wave are found as described in Section 2. It is easy to establish a lower bound for v. Indeed, because the vaporization rate is fast, the temperature cannot exceed the boiling point, $\theta < 1$. Applying the criterion $\theta^- < 1$ to the upstream value (2.26), we find

$$v > v_{min} = q_r Y_o^{inj} - q_v Y_h^{eq}(0)\Psi_g^+ + \alpha_g. \tag{6.1}$$

The first term on the right-hand side (related to the reaction heat) provides the main contribution, while the other two terms are small corrections; Ψ_g^+ is determined by (2.25).

For the reservoir data studied in Section 4, we recomputed the ratio v/u^{inj} and the downstream liquid saturation s_l^+ using the lower limit $v = v_{min}$ for the MTO wave speed in (6.1). The results are shown by thin lines in the left plot of Figs. 5 and 6. One can see that the decrease of the wave speed and of the downstream liquid saturation (up to about 30% and 10%, respectively) are

possible due to diffusion and capillary forces. Therefore, large diffusion and capillary forces lead to moderate changes of MTO wave parameters, lowering the temperatures and decreasing effectiveness of the MTO wave for oil displacement.

7 Conclusion

A model was proposed to study medium temperature light oil combustion (MTO) in porous media. The medium temperature is roughly between the temperatures for low temperature oxidation, where oxygenated hydrocarbons are formed, and high temperature oxidation that is concerned with coke combustion. The MTO reaction is assumed to be slow, so that vaporization is much faster, and a local equilibrium model suffices. The model considers light oil recovery when it is displaced by air at medium pressures in a linear geometry, for the case when water is absent. The liquid oil reacts with oxygen according to simple rate equations. This very simple model can be used to deliver some essential insights. The details of the reaction rate equation have no effect on the global result. Vaporization occurs upstream of the combustion zone. For all cases of practical interest the vaporization wave and combustion wave move at the same speed, which is a manifestation of resonance. The state of resonance can be found by solving seven non-linear algebraic equations.

MTO combustion displaces all the oil, inclusive residual oil at a cost of small amounts of burned oil. In the initial period the recovery curve is similar to Buckley-Leverett gas displacement, but after a critical amount of air has been injected, the cumulative oil recovery increases linearly until all oil has been recovered. It turns out that the recovery using combustion is much faster than for gas injection without combustion displacement. Finally the recovery is slower for higher boiling point and viscosity of oil, but faster at higher injection pressure. We used a simple fractional flow procedure to compute recovery curves for a variety of different conditions. It can be shown that incorporation of capillary pressure effects, longitudinal heat conduction effects and molar mass diffusion effects in the model do not alter the fractional flow results significantly. It would be desirable in the future to include water.

Acknowledgments

This research was carried out within the context of the ISAPP Knowledge Centre. ISAPP (Integrated Systems Approach to Petroleum Production) is a joint project of the Netherlands Organization of Applied Scientific Research TNO, Shell International Exploration and Production, and Delft University of Technology. The paper was also supported by grants of PRH32 (ANP 731948/2010, PETROBRAS 6000.0061847.10.4), FAPERJ (E-26/102.965/2011, E-26/111.416 /2010, E-26/110.658/2012, E-26/110.237/2012, E-26/111.369/2012) and CNPq (301564/2009-4, 472923/2010-2, 477907/2011-3, 305519/2012-3, 402299/2012-4, 470635/2012-6). The authors thank TU Delft and IMPA for providing the opportunity for this work.

Nomenclature

A_r	MTO pre-exponential factor, 1/s
c_l, c_g	heat capacity of liquid and gas, J/(mol·K)
C_m	heat capacity of porous rock, J/(m^{3}K)
D	gas diffusion coefficient, m^2/s
f_l	fractional flow function for liquid phase
J	Leverett J-function
k	rock permeability, m^2
k_l, k_g	liquid and gas phase permeabilities, m^2
k_e	rate constant for evaporation, mol/(m$^3 s$)
n	MTO reaction order with respect to oxygen
P_g	prevailing gas pressure, Pa
Q_r	MTO reaction enthalpy per mole of oxygen at reservoir temperature, J/mol
Q_v	oil vaporization heat at reservoir temperature, J/mol
R	ideal gas constant, J/(mol·K)
s_l, s_g	saturations of liquid and gas phases
t	time, s
T	temperature, K
T^b	boiling temperature of liquid, K
T^{ini}	reservoir temperature, K
T^{ac}	MTO activation temperature, K
u_l, u_g, u	liquid, gas and total Darcy velocities, m/s
u_{gj}	Darcy velocity of component $j = h, o, r$ in gas phase, m/s
u_g^{inj}	injection Darcy velocity of gas, m/s
W_v, W_r	vaporization and MTO reaction rates, mol/(m$^3 s$)
x	spatial coordinate, m
Y_h, Y_o, Y_r	gas molar fractions: hydrocarbons, oxygen, remaining components, mol/mol
Y_o^{inj}	oxygen fraction in injected gas
φ	porosity
λ	thermal conductivity of porous medium, W/(m·K)
μ_l, μ_g	viscosity of liquid and gas, Pa·s
ν_l, ν_g	stoichiometric coefficients in the MTO reaction (1.1)
ρ_l, ρ_g	molar density of liquid and gas, mol/m^3
σ	liquid oil surface tension, N/m
Θ	liquid oil/rock contact angle

References

[1] J. H. Abou-Kassem, S. M. Farouq Ali, and J. Ferrer. Appraisal of steamflood models. *Rev. Tec. Ing.*, 9:45–58, 1986.

[2] S. Akin, M.V. Kok, S. Bagci, and O. Karacan. Oxidation of heavy oil and their SARA fractions: its role in modeling in-situ combustion. SPE 63230, 2000.

[3] A. Bakry, A. Al-Salaymeh, A.H. Al-Muhtaseb, A. Abu-Jrai, and D. Trimis. Adiabatic premixed combustion in a gaseous fuel porous inert media under high pressure and temperature: Novel flame stabilization technique. *Fuel*, 90(2):647–658, 2011.

[4] Y. Barzin, R. Moore, S. Mehta, D. Mallory, M. Ursenbach, and F. Tabasinejad. Role of vapor phase in oxidation/combustion kinetics of high-pressure air injection (HPAI). In *SPE 135641*, 2010.

[5] Y. Barzin, R. Moore, S. Mehta, M. Ursenbach, and F. Tabasinejad. Impact of Distillation on the Combustion Kinetics of high pressure air injection (HPAI). In *SPE 129691-Improved Oil Recovery Symposium*, 2010.

[6] A. Bayliss and B.J. Matkowsky. From traveling waves to chaos in combustion. *SIAM J. Appl. Math.*, 54:147–174, 1994.

[7] R.B. Bird, W.E. Stewart, and E.N. Lightfoot. Transport Phenomena, 2002.

[8] A.A. Boxerman and M.F. Yambaev. In-situ air transformation process into a light-oil reservoir. In *12th European Symposium on Improved Oil Recovery*, 2003.

[9] J. Bruining, A.A. Mailybaev, and D. Marchesin. Filtration combustion in wet porous medium. *SIAM J. Appl. Math.*, 70:1157–1177, 2009.

[10] L.M. Castanier and W.E. Brigham. Modifying in-situ combustion with metallic additives. *In Situ*, 21(1):27–45, 1997.

[11] L.M. Castanier and W.E. Brigham. Upgrading of crude oil via in situ combustion. *Journal of Petroleum Science and Engineering*, 39:125–136, 2003.

[12] L.P. Dake. *Fundamentals of reservoir engineering*. Elsevier Science, 1978.

[13] A. De Zwart, D. van Batenburg, C. Blom, A. Tsolakidis, C. Glandt, and P. Boerrigter. The modeling challenge of high pressure air injection. In *SPE/DOE Symposium on Improved Oil Recovery*, 2008.

[14] M. Fassihi, W. Brigham, and H. Ramey Jr. Reaction kinetics of in-situ combustion: part 2–modeling. *Old SPE Journal*, 24(4):408–416, 1984.

[15] M.R. Fassihi, D.V. Yannimaras, and V.K. Kumar. Estimation of recovery factor in light-oil air-injection projects. *SPE Reservoir Engineering*, 12:173–178, 1997.

[16] W. Fickett and W.C. Davis. *Detonation: theory and experiment*. Dover, Mineola, N.Y., 2011.

[17] N.P. Freitag and B. Verkoczy. Low-temperature oxidation of oils in terms of SARA fractions: why simple reaction models don't work. *Journal of Canadian Petroleum Technology*, 44(3):54–61, 2005.

[18] P. Germain and J.L. Geyelin. Air injection into a light oil reservoir: the horse creek project. In *Middle East Oil Show and Conference*, 1997.

[19] M. Gerritsen, A. Kovscek, L. Castanier, J. Nilsson, R. Younis, and B. He. Experimental investigation and high resolution simulator of in-situ combustion processes; 1. simulator design and improved combustion with metallic additives. In *SPE International Thermal Operations and Heavy Oil Symposium and Western Regional Meeting*, 2004.

[20] T.H. Gillham, B.W. Cerveny, M.A. Fornea, and D. Bassiouni. Low cost IOR: an update on the W. Hackberry air injection project. In *Paper SPE-39642 presented at the SPE/DOE Improved Oil Recovery Symposium, Tulsa, Oklahoma, April, 19–22*, 1998.

[21] T.H. Gillham, B.W. Cerveny, E.A. Turek, and D.V. Yannimaras. Keys to increasing production via air injection in gulf coast light oil reservoirs. In *SPE Annual Technical Conference and Exhibition, SPE 38848-MS*, 1997.

[22] M. Greaves, S. Ren, R. Rathbone, T. Fishlock, and R. Ireland. Improved residual light oil recovery by air injection (LTO process). *Journal of Canadian Petroleum Technology*, 39(1), 2000.

[23] M. Greaves, T.J. Young, S. El-Usta, R.R. Rathbone, S.R. Ren, and T.X. Xia. Air injection into light and medium heavy oil reservoirs: combustion tube studies on West of Shetlands Clair oil and light Australian oil. *Chemical Engineering Research and Design*, 78(5):721–730, 2000.

[24] D. Gutierrez, F. Skoreyko, R. Moore, S. Mehta, and M. Ursenbach. The challenge of predicting field performance of air injection projects based on laboratory and numerical modelling. *Journal of Canadian Petroleum Technology*, 48(4):23–33, 2009.

[25] D. Gutierrez, A. Taylor, V. Kumar, M. Ursenbach, R. Moore, and S. Mehta. Recovery factors in high-pressure air injection projects revisited. *SPE Reservoir Evaluation & Engineering*, 11(6):1097–1106, 2008.

[26] W.C. Hardy, P.B. Fletcher, J.C. Shepard, E.W. Dittman, and D.W. Zadow. In-situ combustion in a thin reservoir containing high-gravity oil. *Journal of Petroleum Technology*, 24(2):199–208, 1972.

[27] J. Harterich. Viscous profiles of traveling waves in scalar balance laws: The canard case. *Methods and Applications of Analysis*, 10(1):97–118, 2003.

[28] F.G. Helfferich. *Kinetics of multistep reactions*, volume 40. Elsevier Science Limited, 2004.

[29] N. Khoshnevis Gargar, N. Achterbergh, S. Rudolph-Flöter, and H. Bruining. In-Situ oil combustion: processes perpendicular to the main gas flow direction. In *SPE Annual Technical Conference and Exhibition*, SPE 134655-MS, 2010.

[30] M.V. Kok and C.O. Karacan. Behavior and effect of SARA fractions of oil during combustion. *SPE Reservoir Evaluation and Engineering*, 3:380–385, 2000.

[31] A.G. Kulikovskii and N.T. Pashchenko. Propagation regimes of self-supported light-detonation waves. *Fluid Dynamics*, 40(5):818–828, 2005.

[32] O. Levenspiel. *Chemical reaction engineering*. John Wiley & Sons, 1999.

[33] C.Y. Lin, W.H. Chen, and W.E. Culham. New kinetic models for thermal cracking of crude oils in in-situ combustion processes. *SPE Reservoir Engineering*, 2:54–66, 1987.

[34] C.Y. Lin, W.H. Chen, S.T. Lee, and W.E. Culham. Numerical simulation of combustion tube experiments and the associated kinetics of in-situ combustion processes. *SPE Journal*, 24:657–666, 1984.

[35] A.A. Mailybaev, J. Bruining, and D. Marchesin. Analysis of in situ combustion of oil with pyrolysis and vaporization. *Combustion and Flame*, 158(6):1097–1108, 2010.

[36] A.A. Mailybaev, J. Bruining, D. Marchesin, S. Rudolph, and T.J. Heimovaara. Cleaning tar deposits by diluted air combustion. In *First International Conference on Frontiers in Shallow Subsurface Technology, Delft, The Netherlands*, 20 – 22 January 2010.

[37] A.A. Mailybaev, D. Marchesin, and J. Bruining. Resonance in low-temperature oxidation waves for porous media. *SIAM Journal on Mathematical Analysis*, 43:2230–2252, 2011.

[38] B.J. Matkowsky and G. Sivashinsky. Propagation of a pulsating reaction front in solid fuel combustion. *SIAM J. Appl. Math.*, 35:465–478, 1978.

[39] A.R. Montes, D. Gutierrez, R.G. Moore, S.A. Mehta, and M.G. Ursenbach. Is high-pressure air injection (HPAI) simply a flue-gas flood? *Journal of Canadian Petroleum Technology*, 49(2):56–63, 2010.

[40] O.A. Oleinik. Construction of a generalized solution of the cauchy problem for a quasi-linear equation of first order by the introduction of vanishing viscosity. *Uspekhi Matematicheskikh Nauk*, 14(2):159–164, 1959.

[41] F.M. Pereira, A.A.M. Oliveira, and F.F. Fachini. Asymptotic analysis of stationary adiabatic premixed flames in porous inert media. *Combustion and Flame*, 156(1):152–165, 2009.

[42] B.E. Poling, J.M. Prausnitz, O.C. John Paul, and R.C. Reid. *The properties of gases and liquids*. McGraw-Hill, New York, 2001.

[43] M. Quintard, L. Bletzacker, D. Chenu, and S. Whitaker. Nonlinear, multicomponent, mass transport in porous media. *Chemical engineering science*, 61(8):2643–2669, 2006.

[44] J. Sanmiguel, D. Mallory, S. Mehta, and R. Moore. Formation heat treatment process by combustion of gases around the wellbore. *Journal of Canadian Petroleum Technology*, 41(8), 2002.

[45] G.L. Schott. Kinetic studies of hydroxyl radicals in shock waves. iii. the OH concentration maximum in the hydrogen-oxygen reaction. *The Journal of Chemical Physics*, 32:710, 1960.

[46] D.A. Schult, B.J. Matkowsky, V.A. Volpert, and A.C. Fernandez-Pello. Forced forward smolder combustion. *Combustion and Flame*, 104:1–26, 1996.

[47] W. Schulte. Challenges and strategy for increased oil recovery. In *International Petroleum Technology Conference*, 2005.

[48] G.J. Sharpe and S. Falle. One-dimensional nonlinear stability of pathological detonations. *Journal of Fluid Mechanics*, 414(1):339–366, 2000.

[49] C.W. Wahle, B.J. Matkowsky, and A.P. Aldushin. Effects of gas-solid nonequilibrium in filtration combustion. *Combust. Sci. and Tech.*, 175:1389–1499, 2003.

[50] H.J. Welge. A simplified method for computing oil recovery by gas or water drive. *Transactions of AIME*, 195:91–98, 1952.

[51] W.W. Wood and Z.W. Salsburg. Analysis of steady-state supported one-dimensional detonations and shocks. *Physics of Fluids*, 3:549–566, 1960.

[52] Z. Xu, L. Jianyi, S. Liangtian, L. Shilun, and L. Weihua. Research on the mechanisms of enhancing recovery of light-oil reservoir by air-injected low-temperature oxidation technique. *Natural Gas Industry*, 24:78–80, 2004.

[53] C.H. Zheng, L.M. Cheng, T. Li, Z.Y. Luo, and K.F. Cen. Filtration combustion characteristics of low calorific gas in sic foams. *Fuel*, 89(9):2331–2337, 2010.